Defense Technical Information Center Compilation Part Notice

ADP013688

TITLE: Large-Eddy Simulation of Mach 3.0 Flow Past a 24-Degree Compression Ramp

DISTRIBUTION: Approved for public release, distribution unlimited

This paper is part of the following report:

TITLE: DNS/LES Progress and Challenges. Proceedings of the Third AFOSR International Conference on DNS/LES

To order the complete compilation report, use: ADA412801

The component part is provided here to allow users access to individually authored sections of proceedings, annals, symposia, etc. However, the component should be considered within the context of the overall compilation report and not as a stand-alone technical report.

The following component part numbers comprise the compilation report:
ADP013620 thru ADP013707

LARGE-EDDY SIMULATION OF MACH 3.0 FLOW PAST A 24-DEGREE COMPRESSION RAMP

DONALD P. RIZZETTA AND MIGUEL R. VISBAL

Air Force Research Laboratory

Wright-Patterson Air Force Base, Ohio 45433-7521

Abstract.

Large-eddy simulation of the Mach 3.0 flow past a 24 deg compression ramp is performed by a high-order numerical method. Spatial derivatives are represented by a sixth-order compact stencil that is used in conjunction with a tenth-order non-dispersive filter. The scheme employs a time-implicit approximately-factored finite-difference algorithm, and applies Newton-like subiterations to achieve second-order temporal and sixth-order spatial accuracy. In the region of the shock wave, compact differencing of convective fluxes is replaced locally by a third-order Roe upwind-biased evaluation. The Smagorinsky dynamic subgrid-scale model is incorporated in the simulation to account for the spatially under-resolved stresses and heat flux. Comparisons are made with experimental data in terms time-mean surface pressure and skin friction distributions, and with instantaneous surface pressure measurements.

1. Introduction

Large-eddy simulation(LES) of supersonic flows is useful for studying compressibility effects, which can appreciably alter fluid physics. Such studies increase the understanding of turbulence mechanisms and can lead to the development, improvement, and testing of lower-order closure models. Despite remaining computationally intensive, LES also may be beneficial in the design and analysis of high-speed flight vehicles and associated propulsion systems where less sophisticated approaches fail.

Due to their geometric simplicity, supersonic compression-ramp flow-fields have been studied extensively, both experimentally and computationally. Characteristics of the unsteady shock-wave motion of such flows

have been observed, measured, and analyzed by Andreopoulos and Muck[1], Smits and Muck[2], Dolling and Murphy[3], and Erengil and Dolling[4, 5], among others. Numerical investigations have typically considered the Reynolds-averaged Navier-Stokes equations used in conjunction with mean turbulence models. These efforts have met with limited success in the prediction of quantities such as heat transfer and skin friction, particularly in situations with large reversed-flow regions[6]. It is believed that this difficulty may be due in part to the disparity between the time-mean and instantaneous shock-system structure. In addition, the models and resultant computations often fail to account for compressibility effects or the three-dimensionality of the flowfield. In an effort to overcome these deficiencies, direct numerical and large-eddy simulations have been carried out by Hunt and Nixon[7], Urbin et al.[8, 9], Adams[10, 11], and Rizzetta et al.[12, 13] The present effort provides a large-eddy simulation for the flow past at 24 deg compression ramp at a freestream Mach number of 3.0 and $Re_\theta = 1696$.

2. Governing Equations

The governing equations are the unsteady three-dimensional compressible Favre filtered Navier-Stokes equations, written in nondimensional variables utilizing a generalized coordinate system, and expressed notationally in the following conservative form

$$\frac{\partial Q}{\partial t} + \frac{\partial}{\partial \xi}(F - \frac{1}{Re}F_v) + \frac{\partial}{\partial \eta}(G - \frac{1}{Re}G_v) + \frac{\partial}{\partial \zeta}(H - \frac{1}{Re}H_v) = 0. \quad (1)$$

All dependent variables may be decomposed into a filtered or large-scale portion, and a subgrid-scale component e.g., $u = \bar{u} + u_{sg}$. It is then convenient for compressible flows to recast the large-scale component in terms of a Favre-averaged variable so that

$$\tilde{u} = \frac{\overline{\rho u}}{\bar{\rho}}. \quad (2)$$

The subgrid-scale stress and heat flux are provided by

$$\tau_{ij} = -Re\bar{\rho}(\widetilde{u_i u_j} - \tilde{u}_i \tilde{u}_j), \quad Q_i = Re\bar{\rho}(\widetilde{u_i T} - \tilde{u}_i \tilde{T}). \quad (3)$$

Following Germano et al.[14], the compressible version of the model is given in trace-free form as

$$\mu_t = ReC\Delta^2\bar{\rho}\tilde{S}_M \quad \text{where} \quad \tilde{S}_M = \left(2\tilde{S}_{ij}\tilde{S}_{ij}\right)^{1/2} \quad (4)$$

is the magnitude of the rate-of-strain tensor, and

$$\tilde{S}_{ij} = \frac{1}{2}\left(\frac{\partial \xi_k}{\partial x_j}\frac{\partial \tilde{u}_i}{\partial \xi_k} + \frac{\partial \xi_k}{\partial x_i}\frac{\partial \tilde{u}_j}{\partial \xi_k}\right). \tag{5}$$

The eddy-viscosity length scale is taken as

$$\Delta = \left(\frac{1}{J}\right)^{1/3} \tag{6}$$

which corresponds to the width of the grid filter in physical space, C is the eddy-viscosity model coefficient, and

$$\tau_{ij} - \frac{1}{3}\tau_{kk}\delta_{ij} = -2\mu_t\left(\tilde{S}_{ij} - \frac{1}{3}\tilde{S}_{kk}\delta_{ij}\right). \tag{7}$$

For compressible applications, the isotropic part of the stress tensor is obtained according to Yoshizawa[15] from

$$\tau_{kk} = 2C_I\Delta^2\bar{\rho}\tilde{S}_M^2. \tag{8}$$

To complete closure of the model, the subgrid-scale heat flux vector is specified in terms of the turbulent Prandtl number as

$$Q_i = -\left(\frac{\mu_t}{Pr_t}\right)\frac{\partial \xi_j}{\partial x_i}\frac{\partial \tilde{T}}{\partial \xi_j}. \tag{9}$$

The model coefficients C, C_I, and the turbulent Prandtl number Pr_t are computed as a function of time and space from the energy content of the resolved large-scale structures.

3. Numerical Method

Time-accurate solutions to Eq. 1 were obtained numerically by the implicit approximately-factored finite-difference algorithm of Beam and Warming[16] employing Newton-like subiterations, which may be represented notationally as follows

$$\left[I + \left(\frac{2\Delta t}{3}\right)\delta_{\xi 2}\left(\frac{\partial F^p}{\partial Q} - \frac{1}{Re}\frac{\partial F_v^p}{\partial Q}\right)\right] \times \tag{10}$$

$$\left[I + \left(\frac{2\Delta t}{3}\right)\delta_{\eta 2}\left(\frac{\partial G^p}{\partial Q} - \frac{1}{Re}\frac{\partial G_v^p}{\partial Q}\right)\right] \times$$

$$\left[I + \left(\frac{2\Delta t}{3}\right)\delta_{\zeta 2}\left(\frac{\partial H^p}{\partial Q} - \frac{1}{Re}\frac{\partial H_v^p}{\partial Q}\right)\right]\Delta Q$$

$$= -\left(\frac{2\Delta t}{3}\right)\left[\left(\frac{1}{2\Delta t}\right)\left(3Q^p - 4Q^n + Q^{n-1}\right)\right.$$
$$+\delta_{\xi 6}\left(F^p - \frac{1}{Re}F_v^p\right) + \delta_{\eta 6}\left(G^p - \frac{1}{Re}G_v^p\right)$$
$$\left.+ \delta_{\zeta 6}\left(H^p - \frac{1}{Re}H_v^p\right)\right].$$

In this expression, which was employed to advance the solution in time, Q^{p+1} is the $p+1$ approximation to Q at the $n+1$ time level Q^{n+1}, and $\Delta Q = Q^{p+1} - Q^p$. The implicit segment of the algorithm incorporated second-order-accurate centered differencing for all spatial derivatives($\delta_{\xi 2}, \delta_{\eta 2}, \delta_{\zeta 2}$), and utilized the diagonalized form of the factorized equations to enhanced efficiency. Temporal and spatial accuracy were maintained by utilizing subiterations within a time step.

A sixth-order tridiagonal subset of Lele's[17] compact difference scheme was used to evaluate the right-hand side of Eq. 10($\delta_{\xi 6}, \delta_{\eta 6}, \delta_{\zeta 6}$), and is illustrated here in one spatial dimension as

$$\alpha\left(\frac{\partial F}{\partial \xi}\right)_{i-1} + \left(\frac{\partial F}{\partial \xi}\right)_i + \alpha\left(\frac{\partial F}{\partial \xi}\right)_{i+1} \tag{11}$$
$$= a\left(\frac{F_{i+1} - F_{i-1}}{2}\right) + b\left(\frac{F_{i+2} - F_{i-2}}{4}\right)$$

$$\text{with} \quad \alpha = 1/3, \quad a = 14/9, \quad b = 1/9. \tag{12}$$

The scheme is used in conjunction with a 10th-order non-dispersive compact spatial filter in order to maintain both stability and accuracy, particularly on stretched curvilinear meshes. The filter is applied to the solution vector sequentially in each of the three computational directions following each subiteration, and is implemented as

$$\alpha_f\check{Q}_{i-1} + \check{Q}_i + \alpha_f\check{Q}_{i+1} = \sum_{n=0}^{5}\frac{a_n}{2}(Q_{i+n} + Q_{i-n}) \tag{13}$$

where $\check{Q}$ is the filtered value of Q. Equation 13 represents a one-parameter family of filters, where numerical values for α_f and the a_n's may be found in Ref.[18]. Repeated application of the spatial filter can result in shock waves that are excessively diffuse. This deficiency is overcome by replacing the compact-differencing of convective derivatives and use of filtering, by Roe's third-order upwind-biased scheme, locally in inviscid regions of shock waves.

4. Results

A computational domain size was taken as

$$L_x = 31.2\delta_0, \quad L_y = 4.7\delta_0, \quad L_z = 2.9\delta_0, \tag{14}$$

where L_x, L_y, L_z, are streamwise, vertical, and spanwise extents respectively, and δ_0 is the height of the incoming boundary layer. The vertical extent L_y corresponds to the domain height at the inflow location. This region was discretized with a nonuniform computational mesh consisting of $(421 \times 151 \times 81)$ points in (i, j, k). At the inflow location, the grid had the following minimum spacings in wall units:

$$\Delta x^+ = 16.8, \quad \Delta y^+ = 1.4, \quad \Delta z^+ = 8.3. \tag{15}$$

Based upon the mean incoming profile, 79 of the 151 vertical grid points were within the boundary layer.

The solution presented here for the Mach 3.0 flow past a 24 deg compression ramp with $Re_\theta = 1696$ represents part of a comprehensive investigation which was performed for supersonic compression-ramp flows. These are described, along with more complete details of the present simulation, in Ref.[13]. Typical instantaneous results at the midspan location are presented in Fig. 1. Mach number contours appear in the left-hand portion of the figure, while the grid structure is indicated to the right. Segments of the grid which are blanked out correspond to mesh points where convective derivatives were obtained via the Roe upwind-biased scheme. In the figure, only every other i-grid and every third j-grid line are displayed. It is evident that the upwind-biased evaluation is confined locally to a small region surrounding the shock wave, so that accuracy of the high-order method is not compromised in other regions of the flowfield.

Although no experimental data exists for the exact flow conditions of the simulation, it is useful to compare to measurements obtained at Reynolds numbers which were several orders of magnitude larger than that of the computation. Spanwise averaged time-mean surface pressure and skin friction coefficient distributions are shown in Fig. 2. The pressure coefficient has been normalized by the inviscid rise to account for variations in the freestream Mach number between the calculation and experiments. Because of the higher Reynolds numbers of the measurements, Cf has been normalized by its value just upstream of the interaction region.

Comparisons of the computed surface pressure standard deviation(s) and skewness(Sk) distributions with the data of Dolling and Murphy[3] appear in Fig. 3. The value of s upstream of the interaction(s_1) has been removed from the standard deviation in order to account for differences in the incoming states between the simulation and the experiment. Apart from

disparities near separation($X/\delta_0 \approx -2.0$), these comparisons are favorable. The disparities are caused by differences in the shock wave motion between the respective results, which will be illustrated subsequently.

The wall pressure intermittency(Γ) and instantaneous pressure time history are displayed in Fig. 4. It is observed that the experimental distributions of Γ have a steeper rise which occurs further downstream than the numerical result. This is due to the more extensive interaction region present in the low Reynolds number large-eddy simulation. Although the time mean level of the computed surface pressure near the separation point is approximately the same as that of the experiment, a very different fluctuating component is indicated. The high frequency oscillations exhibited in the numerical simulation are similar to those of the incoming boundary layer, while the low frequency modes of the experiment correspond to more extensive motion of the shock wave.

5. Summary

Computed surface pressure and skin friction distributions compared reasonably well with experimental data collected at higher Reynolds numbers. Comparisons were also made with statistical quantities extracted from instantaneous unsteady surface pressure measurements.

6. Acknowledgments

References

1. Andreopoulos, J., and Muck, K. C., "Some New Aspects of the Shock-Wave/Boundary-Layer Interaction in Compression-Ramp Flows," *Journal of Fluid Mechanics*, Vol. 180, July 1987, pp. 405-428.
2. Smits, A. J., and Muck, K.-C., "Experimental Study of Three Shock Wave / Turbulent Boundary Layer Interactions," *Journal of Fluid Mechanics*, Vol. 182, Sept. 1987, pp. 291-314.
3. Dolling, D. S., and Murphy, M. T., "Unsteadiness of the Separation Shock Wave Structure in a Supersonic Compression Ramp Flowfield," *AIAA Journal*, Vol. 23, No. 12, Dec. 1983, pp. 1628-1634.
4. Erengil, E. E., and Dolling, D. S., "Unsteady Wave Structure Near Separation in a Mach 5 Compression Ramp Interaction," *AIAA Journal*, Vol. 29, No. 5, May 1990, pp. 728-735.

5. Erengil, M. E., and Dolling, D. S., "Correlation of Separation Shock Motion with Pressure Fluctuations in the Incoming Boundary Layer," *AIAA Journal*, Vol. 29, No. 11, Nov. 1991, pp. 1868-1877.
6. Settles, G. S., Fitzpatrick, T. J., and Bogdonoff, S. M., "Detailed Study of Attached and Separated Compression Corner Flowfields in High Reynolds Number Supersonic Flow," *AIAA Journal*, Vol. 17, No. 6, June 1979, pp. 579-585.
7. Hunt, D., and Nixon, D., "A Very Large Eddy Simulation of an Unsteady Shock Wave Turbulent Boundary Layer Interaction," AIAA Paper 95-2212, June 1995.
8. Urbin, G., Knight, D., and Zheltovodov, A. A., "Compressible Large Eddy Simulation using Unstructured Grid: Supersonic Turbulent Boundary Layer and Compression Corner," AIAA Paper 99-0427, Jan. 1999.
9. Urbin, G., Knight, D., and Zheltovodov, A. A., "Large Eddy Simulation of a Supersonic Compression Corner Part I," AIAA Paper 2000-0398, Jan. 2000.
10. Adams, N. A., "Direct Numerical Simulation of Turbulent Compression Ramp Flow," *Theoretical and Computational Fluid Dynamics*, Vol. 12, No. 2, Sept. 1998, pp. 109-129.
11. Adams, N. A., "Direct Simulation of the Turbulent Boundary Layer along a Compression Ramp at $M = 3$ and $Re_\theta = 1685$," *Journal of Fluid Mechanics*, Vol. 420, Oct. 2000, pp. 47-83.
12. Rizzetta, D. P., Visbal, M. R., and Gaitonde, D. V., "Direct Numerical and Large-Eddy Simulation of Supersonic Flows by a High-Order Method," AIAA Paper 2000-2408, June 2000.
13. Rizzetta, D. P., and Visbal, M. R., "Large-Eddy Simulation of Supersonic Compression-Ramp Flows," AIAA Paper 2001-2858, June 2001.
14. Germano, M., Piomelli, U., Moin, P., and Cabot, W. H., "A Dynamic Subgrid-Scale Eddy Viscosity Model," *Physics of Fluids A*, Vol. 3, No. 7, July 1991, pp. 1760-1765.
15. Yoshizawa, A., "Statistical Theory for Compressible Turbulent Shear Flows, with the Application to Subgrid Modeling," *Physics of Fluids*, Vol. 29, No. 7, July 1986, pp. 2152-2164.
16. Beam, R., and Warming, R., "An Implicit Factored Scheme for the Compressible Navier-Stokes Equations," *AIAA Journal*, Vol. 16, No. 4, Apr. 1978, pp. 393-402.
17. Lele, S. A., "Compact Finite Difference Schemes with Spectral-like Resolution," *Journal of Computational Physics*, Vol. 103, No. 1, Nov. 1992, pp. 16-42.
18. Gaitonde, D., and Visbal, M. R., "High-Order Schemes for Navier-Stokes Equations: Algorithm and Implementation into FDL3DI," AFRL-VA-WP-TR-1998-3060, Wright-Patterson AFB, OH, Aug. 1998.
19. Settles, G. S., and Dodson, L. J., "Hypersonic Shock/Boundary-Layer Interaction Database: New and Corrected Data," NASA-CR-177638, Apr. 1994.
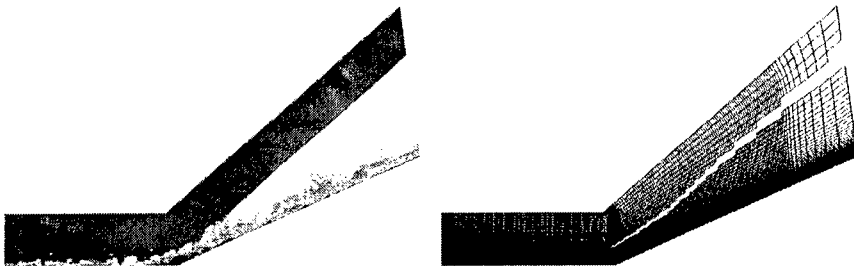
Figure 1. Typical instantaneous Mach number contours and shock-capturing stencils at the midspan location
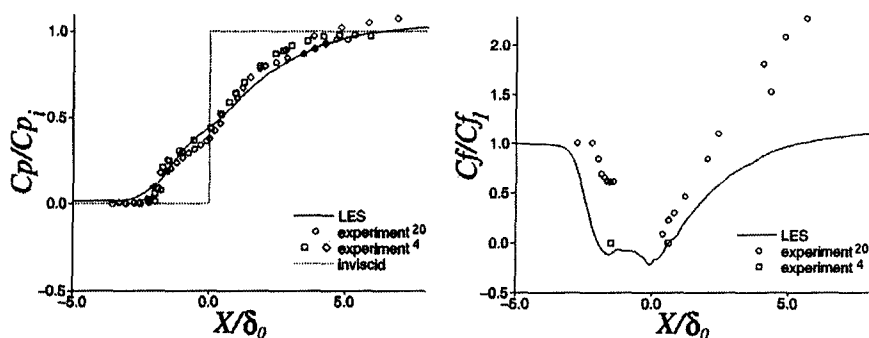
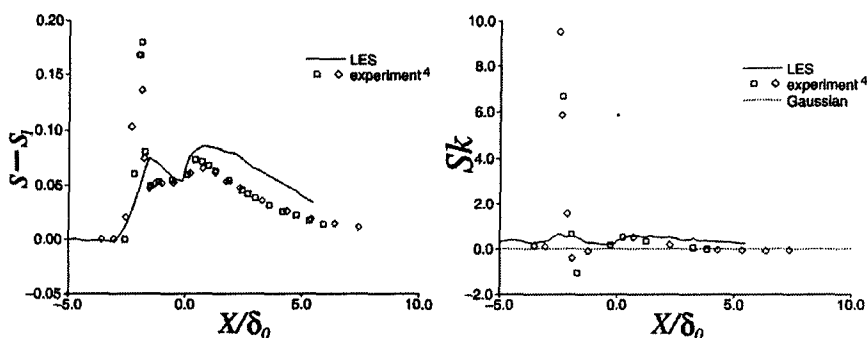*Figure 2.* Spanwise averaged time-mean surface pressure and skin friction coefficient distributions

Figure 3. Spanwise averaged surface pressure standard deviation and skewness distributions
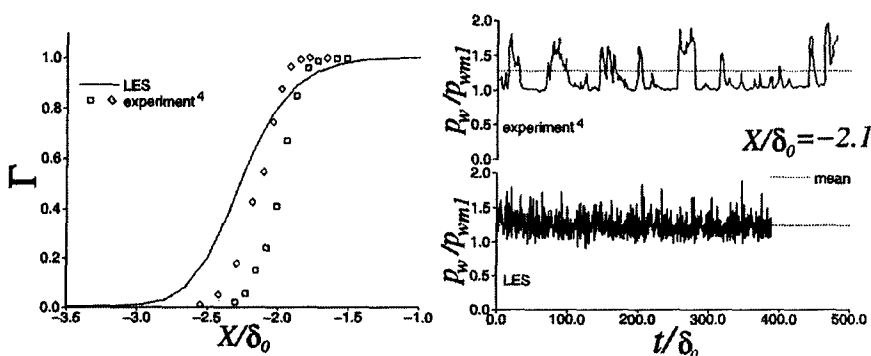

Figure 4. Spanwise averaged surface pressure intermittency distributions and midspan surface pressure time history at $X/\delta_0 = -2.1$